

RESEARCH ARTICLE

A Novel Bayesian Approach with Conditional Autoregressive Specification for Intravoxel Incoherent Motion Diffusion-Weighted MRI

Ettore Lanzarone¹ | Alfonso Mastropietro^{2,3} | Elisa Scalco^{*2,3} | Antonello Vidiri⁴ | Giovanna Rizzo^{2,3}

¹Institute for Applied Mathematics and Information Technologies (IMATI-CNR), Milan, Italy

²Institute of Biomedical Technologies (ITB-CNR), Segrate (MI), Italy

³Institute of Molecular Bioimaging and Physiology (IBFM-CNR), Segrate (MI), Italy

⁴Radiology and Diagnostic Imaging Department, IRCCS Regina Elena National Cancer Institute, Rome, Italy

Correspondence

Elisa Scalco

ITB-CNR

Via Fratelli Cervi, 93

20090 Segrate (MI), Italy

Email: elisa.scalco@itb.cnr.it

Summary

The Intra-Voxel Incoherent Motion (IVIM) model is largely adopted to estimate slow and fast diffusion coefficients of water molecules in biological tissues, which are used in cancer applications. The most reported fitting approach is a voxel-wise segmented non-linear least square, whereas Bayesian approaches with a direct fit, also considering spatial regularization, were proposed too. In this work a novel segmented Bayesian method was proposed, also in combination with a spatial regularization through a Conditional Autoregressive (CAR) prior specification. The two segmented Bayesian approaches, with and without CAR specification, were compared with two standard least-square and a direct Bayesian fitting methods. All approaches were tested on simulated images and real data of patients with head-and-neck and rectal cancer. Estimation accuracy and maps noisiness were quantified on simulated images, whereas the coefficient of variation and the goodness of fit were evaluated for real data. Both versions of the segmented Bayesian approach outperformed the standard methods on simulated images for pseudo-diffusion (D^*) and perfusion fraction (f), whilst the segmented least-square fitting remained the less biased for the diffusion coefficient (D). On real data, Bayesian approaches provided the less noisy maps, and the two Bayesian methods without CAR generally estimated lower values for f and D^* coefficients with respect to the other approaches. The proposed segmented Bayesian approaches were superior, in terms of estimation accuracy and maps quality, to the direct Bayesian model and the least-square fittings. The CAR method improved the estimation accuracy, especially for D^* .

Word count = 7200

Running Head: Novel Bayesian approach with CAR specification for IVIM MRI

KEYWORDS:

IVIM, Diffusion-Weighted MRI, Bayesian Segmented Approach, Conditional Autoregressive Model

1 | INTRODUCTION

Diffusion-Weighted Magnetic Resonance Imaging (DW-MRI) is a non-invasive technique that quantitatively characterizes the diffusion properties of water molecules¹.

⁰**Abbreviations:** CAR, Conditional Autoregressive; CV, Coefficient of Variation; HN, head and neck; LSQ, Least Square; MAE, Mean of Absolute Error; MCMC, Markov Chain Monte Carlo MRF, Markov Random Field; RMSE, Root Mean Square Error; SNR, Signal to Noise Ratio;

Typically, the standard analysis of DW-MRI signals provides the estimation of the Apparent Diffusion Coefficient (ADC), which is estimated using a mono-exponential decay model of the signal intensity over b values.

The Intra-Voxel Incoherent Motion (IVIM) model describes the incoherent motion of the water molecules in function of diffusion and perfusion properties of a tissue at the same time². In the IVIM model, the signal intensity in each voxel is modeled via a bi-exponential decay over b , characterized by a first fast component, which is related to tissue perfusion (the blood flow in the capillaries), followed by a second slow component, which is related to tissue molecular diffusion. Specifically, the IVIM model allows to estimate the diffusion coefficient (D), the pseudo-diffusion coefficient (D^*) and the perfusion volume fraction (f) within the tissue. The estimation of these coefficients can be made within a region of interest, by averaging the signal intensities over the voxels, or voxel-by-voxel to obtain parametric maps.

The tissue characterization through diffusion and perfusion properties has shown promising results, especially in the tumor diagnosis, where tumor identification and grading can be improved by this technique with respect to standard diagnosis^{3,4,5}. In patients affected by rectal cancer, IVIM was proposed for discriminating between good and poor responders to combined chemotherapy and radiation therapy⁶. For the diagnosis of head-and-neck (HN) cancer, it has been shown that the combined use of D and D^* can increase the diagnostic accuracy in predicting malignancy in HN masses with respect to the ADC^{7,8}. In addition, IVIM can also be useful to assess the effect of radiotherapy in normal tissues, since they are usually irradiated during the treatment^{9,10,11}.

The most reported approach for the estimation of D , D^* and f in clinical research is a non-linear least square fitting of the IVIM signal on a voxel-wise basis, where the optimization algorithms classically employed are Levenberg-Marquardt^{12,13} and Trust Region^{14,15} strategies. However, the goodness of fit of such a standard approach is strongly influenced by Signal-to-Noise Ratio (SNR) of the data, especially for the estimation of D^* , making it difficult to assess small localized regions. To overcome this limit, a segmented fitting was generally adopted^{16,17,18}, where D is firstly estimated by considering only the DW-MRI signal at high b values. However, despite the goodness of fit is improved with respect to the direct estimation without segmentation, f and D^* parametric maps remain strongly corrupted by noise¹⁹.

Bayesian approaches were proposed to improve the quality of the parametric maps with a direct fit²⁰, because they allow to use prior information to regularize the fitting. It has been shown that the Bayesian estimation is associated with lower variability and higher precision and accuracy with respect to several least-square approaches²¹. Bayesian approaches also allow to introduce a spatial dependency between voxels. For example, a spatial homogeneity prior was proposed in the form of a continuous Markov random field (MRF), using a *fusion bootstrap moves* algorithm to get the posterior density of the coefficients^{22,23}. Recently, some works compared several estimation approaches of the IVIM parametric maps^{21,19,24,25}, including the standard least-square fittings, the Bayesian model with a Gaussian shrinkage prior²⁶ and the Bayesian model with a spatial homogeneity prior^{22,23,19}. They highlighted that Bayesian approaches consistently outperformed the classical non-linear least square fitting, and that the use of a spatial homogeneity prior can reduce errors with respect to a Gaussian one.

The aim of this work is to propose an alternative Bayesian approach, based on a segmented version of the classical models, for the estimation of smoothed and reliable IVIM maps. This approach should combine the advantages of the standard least-square segmented approach with the improvements of the Bayesian modeling. Two versions of the segmented Bayesian approach are proposed, where the latter includes a spatial regularization in the prior density through a Conditional Autoregressive (CAR) specification that takes into account information from the neighbor voxels. These methods are compared with standard approaches, i.e., the direct and segmented least-square fitting and a classical Bayesian method with Gaussian prior, and tested on both synthetic images and real data of patients with HN and rectal cancer.

2 | METHODS

The signal intensity in voxel (i, j) at a given b value is denoted by $SI(i, j, b)$, and the intensity decay over b is described in each voxel according to the IVIM model of Le Bihan²:

$$SI(i, j, b) = SI(i, j, 0) \left\{ f(i, j) e^{-b[D(i, j) + D^*(i, j)]} + [1 - f(i, j)] e^{-bD(i, j)} \right\} \quad \forall i \in I, j \in J, b \in B \setminus \{0\} \quad (1)$$

The IVIM model with the sum of D and D^* for the first exponential decay² is here preferred to the alternative one, where only D^* appears in the first exponential decay, to have a more direct comparison with other literature works^{19,22,23}.

The goal is to estimate the coefficients $D(i, j)$, $D^*(i, j)$ and $f(i, j) \forall (i, j)$ based on a set of observations SI_{ij}^{obs} for $SI(i, j, b)$ at different b values. Three benchmark models from the literature, i.e., the direct Least Square approach (LSQ-FULL), the Segmented Least Square approach (LSQ-SEG) and the Bayesian Gaussian approach (GAUSS-FULL), are first presented; then, the new approaches proposed in this work, i.e., the Bayesian Segmented Gaussian approach (GAUSS-SEG) and the Bayesian Segmented Conditional Autoregressive approach (CAR), are detailed.

2.1 | Least Square approaches

In both the LSQ-FULL and LSQ-SEG approaches, model (1) is considered and the signal data are fitted voxel by voxel using a Trust Region algorithm²⁷, with the boundary constraints and the function tolerance reported in¹⁹ ($0.0005 < f < 0.9995$; $0.045 < D < 18 [\times 10^{-3} \text{mm}^2/\text{s}]$; $0.34 < D^* < 1000 [\times 10^{-3} \text{mm}^2/\text{s}]$; function tolerance = 10^{-7}). With respect to the LSQ-FULL, a two-step fitting is considered in the LSQ-SEG; D is first estimated using a mono-exponential diffusion model, only considering data for $b \geq \hat{b} = 200 \text{ s}/\text{mm}^2$, in which the diffusion component accounts for a large portion of the measured signal¹⁶. Then, D is kept fixed and the IVIM bi-exponential model is fitted for all b values. Both the LSQ methods are implemented in a custom-made MATLAB routine (MathWorks, Natick, MA, USA).

2.2 | Bayesian approaches

In the non-segmented approach GAUSS-FULL, the following modified version of the IVIM model (1) is considered, in which the sum $D(i, j) + D^*(i, j)$ is condensed in only one parameter $D_{\text{sum}}(i, j)$ that is directly estimated.

$$SI(i, j, b) = SI(i, j, 0) \left\{ f(i, j) e^{-b D_{\text{sum}}(i, j)} + [1 - f(i, j)] e^{-b D(i, j)} \right\} \quad \forall i \in I, j \in J, b \in B \setminus \{0\} \quad (2)$$

Parameters $D^*(i, j)$ are then obtained as $D^*(i, j) = D_{\text{sum}}(i, j) - D(i, j)$. This modified model, which gives the same identification problem and has been already considered in the literature for non-segmented approaches²⁸, is used to reduce model complexity and simplify the computation.

In the segmented approaches GAUSS-SEG and CAR, the estimation procedure is divided in two steps. In the first step, the parameters $D(i, j)$ and $\tilde{f}(i, j)$, where $\tilde{f}(i, j)$ denotes a first estimation of $f(i, j)$, are estimated with the observations at $b = 0$ and $b \in B : b \geq \hat{b}$. A simplified version of the IVIM model (1) is considered, in which the first exponential trend disappears:

$$SI(i, j, b) = SI(i, j, 0) \left[1 - \tilde{f}(i, j) \right] e^{-b D(i, j)} \quad \forall i \in I, j \in J, b \in B : b \geq \hat{b} \quad (3)$$

In the second step, as in the LSQ-SEG approach²⁷, the parameters $D^*(i, j)$ and $f(i, j)$ are estimated using all observations and the complete IVIM model (1), fixing the parameters $D(i, j)$ at the values obtained from the first step (expected value of each marginal posterior density).

The sampling of the posterior density is performed through the Hamiltonian Monte Carlo approach²⁹, by implementing all Bayesian approaches in R with package STAN³⁰, which directly provides the posterior marginal densities of each parameter. Chains are initialized with the mean value of the prior density for each parameter, and samples are obtained considering 1000 iterations after a warm up of 1000 iterations, which allowed the convergence of the chains in all tests. Codes are available as Supporting Information.

2.2.1 | Bayesian Gaussian approach (GAUSS-FULL)

The modified IVIM model (2) is considered, as this is a non-segmented approach, and the parameters to estimate are included in the set Θ , i.e., $\Theta = \mathbf{D} \cup \mathbf{D}_{\text{sum}} \cup \mathbf{f}$ with $\mathbf{D} = \{D(i, j), i \in I, j \in J\}$, $\mathbf{D}_{\text{sum}} = \{D_{\text{sum}}(i, j), i \in I, j \in J\}$ and $\mathbf{f} = \{f(i, j), i \in I, j \in J\}$.

Likelihood function

Each parameter in Θ is assumed to be a random variable. Thus, each decay equation (2) is a random process and the density of each $SI(i, j, b)$ is expressed as conditioned to $D(i, j)$, $D_{\text{sum}}(i, j)$ and $f(i, j)$:

$$SI(i, j, b) \sim \mathcal{L}_{\text{sum}}(SI(i, j, b) | D(i, j), D_{\text{sum}}(i, j), f(i, j), SI(i, j, 0)) \quad \forall i \in I, j \in J, b \in B \setminus \{0\} \quad (4)$$

where \mathcal{L}_{sum} denotes the conditional probability law based on the modified IVIM model (2).

Moreover, all observations SI_{ijb}^{obs} are assumed to be subject to an error, e.g., a measurement error, and thus modeled as stochastic variables. For the observations with $b > 0$, a Gaussian distribution \mathcal{N} with mean value $SI(i, j, b)$ computed by (4) and standard deviation σ_{lk} is adopted:

$$SI_{ijb}^{\text{obs}} \sim \mathcal{N}(SI(i, j, b), \sigma_{lk}^2) \quad \forall i \in I, j \in J, b \in B \setminus \{0\} \quad (5)$$

Then, the values $SI(i, j, 0)$ used in the IVIM model to compute the other $SI(i, j, b)$ values are assumed to follow another Gaussian distribution with mean value SI_{ij0}^{obs} and standard deviation σ_{lk} , similar to the approach adopted in²⁶:

$$SI(i, j, 0) \sim \mathcal{N}(SI_{ij0}^{\text{obs}}, \sigma_{lk}^2) \quad \forall i \in I, j \in J \quad (6)$$

Finally, σ_{lk} is not fixed, as it is not possible to get a fair estimation directly from the acquired maps, but considered as another parameter to estimate, given in terms of a prior distribution.

Actually, a Rician distribution should be used in case of magnitude data for low SNR, while for high SNR the Rician distribution is well approximated by the Gaussian one³¹. Nonetheless, the Gaussian and the Rician likelihood functions were found to give similar results for a large range of SNR³². Thus, a Gaussian noise is applied.

The combination of (4) and (5) gives the conditional law of each observation $SI_{i,j,b}^{obs}$, and their product over $i \in I, j \in J$ and $b \in B \setminus \{0\}$ gives the likelihood function, which depends on Θ and σ_{lk} .

Prior density

A *a priori* independence between each $D(i, j)$, $D_{sum}(i, j)$ and $f(i, j)$ is assumed, and a truncated Gaussian prior distribution is considered for each parameter λ , where λ generically denotes $D(i, j)$, $D_{sum}(i, j)$ or $f(i, j)$. Thus:

$$\lambda \sim \mathcal{N}_{(\lambda_{min}, \lambda_{max})}(\mu_\lambda, \sigma_{0\lambda}^2) \quad (7)$$

The values of the hyper-parameters are $\mu_f = \sigma_{0f} = 0.1$, $\mu_D = \sigma_{0D} = 0.001\text{mm}^2/\text{s}$ and $\mu_{D_{sum}} = \sigma_{0D_{sum}} = 0.011\text{mm}^2/\text{s}$. Values μ_λ are chosen to center the priors on values with the same order of magnitude than those reported in the literature, as already considered in previous works²¹, while $\sigma_{0\lambda} = \mu_\lambda$ defines large densities. Moreover, the priors for D and D_{sum} are truncated in the interval $(0, +\infty)$, to ensure positivity²⁶, while the prior for f in the interval $(0, 0.5)$, which largely covers its range of variability. The upper limit equal to 0.5 introduces an asymmetry in the model, which allows to directly obtain D and D_{sum} without assigning the lowest value to D in each voxel. These priors reflect two features commonly considered in the literature, i.e., a distribution with a modal value and a positive support; in the absence of a widely recognized standard³², the simplest choice is in our opinion a truncated Gaussian density.

Finally, the standard deviation σ_{lk} follows an independent Gamma density to respect its positivity. Scale parameter equal to 1 is assumed to set a large density (in the absence of precise information), and mean value is set to half of the average value of SI_{ij0}^{obs} over $i \in I, j \in J$:

$$\sigma_{lk} \sim \text{Gamma}\left(\frac{\sum_{i \in I, j \in J} SI_{ij0}^{obs}}{2 |I \times J|}, 1\right) \quad (8)$$

2.2.2 | Bayesian Segmented Gaussian approach (GAUSS-SEG)

The estimation procedure is divided in two steps, as this is a segmented approach, and the IVIM models in (3) and (1) are considered for the first and the second step, respectively.

First step

The parameters to estimate at the first step are included in the set Θ_1 , i.e., $\Theta_1 = \mathbf{D} \cup \tilde{\mathbf{f}}$ with $\mathbf{D} = \{D(i, j), i \in I, j \in J\}$ and $\tilde{\mathbf{f}} = \{\tilde{f}(i, j), i \in I, j \in J\}$.

As in the GAUSS-FULL approach, each parameter in Θ_1 is assumed to be a random variable. Thus:

$$SI(i, j, b) \sim \mathcal{L}_{simp}\left(SI(i, j, b) | D(i, j), \tilde{f}(i, j), SI(i, j, 0)\right) \quad \forall i \in I, j \in J, b \in B : b \geq \hat{b} \quad (9)$$

where \mathcal{L}_{simp} denotes the conditional probability law based on the simplified IVIM model (3).

Again, all observations SI_{ijb}^{obs} are assumed to be subject to an error and modeled as stochastic variables. As in (5), Gaussian distributions with mean value $SI(i, j, b)$ and standard deviation σ_{lk} are adopted for the observations with $b \geq \hat{b}$. Then, as in (6), the values $SI(i, j, 0)$ used to compute the other $SI(i, j, b)$ values are assumed to follow another Gaussian distribution with mean value SI_{ij0}^{obs} and standard deviation σ_{lk} .

The combination of (9) and (5) gives the conditional law of each observation $SI_{i,j,b}^{obs}$, and their product over $i \in I, j \in J$ and $b \in B : b \geq \hat{b}$ gives the likelihood function, which depends on Θ_1 and σ_{lk} .

As for the prior, *a priori* independence between each $D(i, j)$ and $\tilde{f}(i, j)$ is again assumed, and a truncated Gaussian prior is considered for each parameter, as in (7). The values of the hyper-parameters are $\mu_{\tilde{f}} = \sigma_{0\tilde{f}} = 0.1$ and $\mu_D = \sigma_{0D} = 0.001\text{mm}^2/\text{s}$, in agreement with those adopted in the GAUSS-FULL approach. The prior for D is truncated in the interval $(0, +\infty)$, while the prior for f in the interval $(0, 0.5)$.

The standard deviation σ_{lk} follows the same prior Gamma density (8) of the GAUSS-FULL approach.

Second step

The parameters to estimate at the second step are included in set Θ_{II} , i.e., $\Theta_{II} = \mathbf{D}^* \cup \mathbf{f}$, where $\mathbf{D}^* = \{D^*(i, j), i \in I, j \in J\}$ and $\mathbf{f} = \{f(i, j), i \in I, j \in J\}$.

All observations are considered, and the parameters $D(i, j)$ assume the expected value of the respective marginal posterior density from the first step. Again, each parameter in Θ_{II} is assumed to be a random variable:

$$SI(i, j, b) \sim \mathcal{L}(SI(i, j, b) | D^*(i, j), f(i, j), SI(i, j, 0)) \quad \forall i \in I, j \in J, b \in B \setminus \{0\} \quad (10)$$

where \mathcal{L} with no subscript denotes the conditional probability law based on the original IVIM model (1).

The same Gaussian distributions for the errors of the observations S_{ij}^{obs} are finally taken. A Gaussian distribution with mean value $SI(i, j, b)$ and standard deviation σ_{1k} is adopted for the observations with $b > 0$, as in (5), while the values $SI(i, j, 0)$ used to compute the other $SI(i, j, b)$ values are assumed to follow another Gaussian distribution with mean value $SI_{i,j,0}^{\text{obs}}$ and standard deviation σ_{1k} , as in (6).

The combination of (10) and (5) gives the conditional law of each observation $S_{i,j,b}^{\text{obs}}$, and their product over $i \in I, j \in J$ and $b \in B \setminus \{0\}$ gives the likelihood function, which depends on Θ_{II} and σ_{1k} .

As for the prior, *a priori* independence between each $D^*(i, j)$ and $f(i, j)$ is again assumed, and a Gaussian prior is considered for each parameter, as in (7). The values of the hyper-parameters are $\mu_f = \sigma_{0f} = 0.1$ and $\mu_{D^*} = \sigma_{0D^*} = 0.01 \text{mm}^2/\text{s}$, in agreement with those adopted in the GAUSS-FULL approach. The prior for D^* is truncated in the interval $(0, +\infty)$, while the prior for f in the interval $(0, 0.5)$. The first estimation \tilde{f} is not considered for defining the prior, as preliminary experiments showed that it is not a better estimation of f with respect to that obtained in the second step by restarting from the Gaussian prior described above.

The standard deviation σ_{1k} follows the same Gamma density (8) of the GAUSS-FULL approach, as in the first step.

2.2.3 | Bayesian Segmented Conditional Autoregressive approach (CAR)

This approach embeds the same decomposition in two steps presented for the GAUSS-SEG, with the same parameter structure (Θ_I and Θ_{II}) and likelihood for each step. The difference with respect to the GAUSS-SEG approach lies in the prior density.

A priori independence between each $D(i, j)$ and $\tilde{f}(i, j)$ (first step) is again assumed, and between each $D^*(i, j)$ and $f(i, j)$ (second step). Then, separately for each parameter λ (where λ generically denotes each parameter in Θ_I or Θ_{II}), a CAR specification is included in the prior. An intrinsic CAR model is considered, in the form proposed by Leroux et al.³³, assuming the following distribution of each parameter given the rest of the values:

$$\lambda(i, j) | \lambda_{i,j}^c \sim \mathcal{N} \left(\frac{\sum_{\alpha \in I, \beta \in J} w(\alpha, \beta, i, j) \lambda(\alpha, \beta)}{\sum_{\alpha \in I, \beta \in J} w(\alpha, \beta, i, j)}, \frac{\sigma_\lambda^2}{\sum_{\alpha \in I, \beta \in J} w(\alpha, \beta, i, j)} \right) \quad (11)$$

where $\lambda_{i,j}^c = \lambda \setminus \{\lambda(i, j)\}$ and $w(\alpha, \beta, i, j)$ denotes the spatial neighborhood matrix. With respect to Leroux et al.³³, the highest value for the spatial association parameter is imposed (equal to 1 and thus not reported in the formula) to get the intrinsic model. As for w , we assume $w(\alpha, \beta, i, j) = 1$ for the voxels (α, β) bordering on (i, j) , and 0 elsewhere:

$$w(\alpha, \beta, i, j) = \begin{cases} 1 & (\alpha, \beta) = \{(i-1, j-1), (i-1, j), (i-1, j+1), (i, j-1), (i, j+1), (i+1, j-1), (i+1, j), (i+1, j+1)\} \\ 0 & \text{otherwise} \end{cases} \quad (12)$$

Then, to smooth the autoregressive component, a mixture model with two components is considered: the above conditional autoregressive specification (11) and the truncated Gaussian density (7) of the GAUSS-FULL and GAUSS-SEG approaches. Thus, the overall prior for each parameter λ , which generically denotes each $D(i, j, b)$ or $\tilde{f}(i, j, b)$ at the first step, and each $D^*(i, j, b)$ or $f(i, j, b)$ at the second step, is a mixture between (11) and (7), with weight 0.75 for the CAR specification (11) and weight 0.25 for the Gaussian component (7).

As for the CAR specification, the priors on the standard deviations are set as follows: $\sigma_{\tilde{f}} \sim \text{Gamma}(0.25, 1)$ and $\sigma_D \sim \text{Gamma}(0.001 \text{mm}^2/\text{s}, 1)$ for the first step; $\sigma_f \sim \text{Gamma}(0.25, 1)$ and $\sigma_{D^*} \sim \text{Gamma}(0.01 \text{mm}^2/\text{s}, 1)$ for the second step. Differently from $\sigma_{0\lambda}$, which are fixed equal to the corresponding mean value, σ_λ are in terms of large prior densities, since we do not have any information about the variability associated with the CAR specification. As for the Gaussian component, the same truncated densities with the same hyper-parameters than in the GAUSS-SEG are chosen. Finally, the standard deviation σ_{1k} follows the same Gamma density of the other approaches.

2.3 | Methods evaluation

All approaches were tested on both simulated images and real clinical data (five patients with HN tumor and four with rectal tumor, as examples of IVIM acquisitions for tumor diagnosis; see Supporting Materials and Supporting Information Tables S1 and S2).

Simulated images were created from bi-dimensional squared parametric maps (128×128 pixels) with three concentric layers that reflect the typical IVIM parameters of three structures: muscles and tumor for both regions; parotid gland in HN images; prostate in pelvic images. The three structures were represented as follows: the muscle in the external layer, the parotid/prostate in the middle layer, and the tumor in the inner layer (see Supporting Information Figure S1). The *true* parameters of each layers were (D [mm^2/s], f , D^* [mm^2/s]): HN muscular tissue (0.0015, 0.066, 0.046); parotid (0.0007, 0.133, 0.036); HN tumor (0.0008, 0.121, 0.017); pelvic muscular tissue (0.0012, 0.178, 0.025); prostate (0.0012, 0.167, 0.007); rectal tumor (0.0011, 0.205, 0.257). These values were chosen according to the literature^{10,34,35} or, in case the information was not available in the literature, such as for the case of obturator muscle, a preliminary estimation was performed from a set of clinical images. The simulated images were generated with the IVIM model, considering $B = \{0, 25, 50, 75, 100, 150, 300, 500, 800\}$ s/ mm^2 for HN and $B = \{0, 25, 50, 75, 100, 300, 600, 1000\}$ s/ mm^2 for pelvis.

Finally, the simulated images were corrupted with a Rician Noise, given by the addition of two Gaussian Noises:

$$SI_{ijb}^{obs} = \sqrt{\left[SI_{ijb}^{sim} + GN_{ijb}\right]^2 + GN_{ijb}^2} \quad \forall i \in I, j \in J, b \in B \quad (13)$$

where SI_{ijb}^{sim} denotes the true simulated value and each Gaussian Noise GN_{ijb} is independently sampled from a Gaussian distribution with null mean value and variance equal to $1/\text{SNR}^2$. The adopted SNR values were 20, 40, 60 and 80.

For the clinical dataset, MR images were acquired using a 1.5-T system (Optima MR 450w, GE Healthcare, Milwaukee, WI, USA). DW-MRI images were obtained by single-shot spin-echo echo-planar imaging with: acquisition matrix equal to 128×128 ; in-plane resolution equal to $1.094 \times 1.094 \text{ mm}^2$; TR/TE equal to 4500ms/72ms for HN and 3500ms/77ms for pelvis; slice thickness equal to 4mm for HN and 5mm for pelvis; same b values as in the simulated images. An average of 4-5 slices that contain the three structures of interest were selected for each patient, excluding basal and apical slices to avoid partial volume effects. In two cases, one structure (the prostate) was not considered since the patients were female. More details are provided in the Supporting Materials and Supporting Information Figure S2.

IVIM coefficients were estimated voxel-by-voxel, and the mean value was calculated within each Region of Interest (ROI).

2.3.1 | Simulated data

The quality of the parametric maps was assessed considering the percent bias (bias) and the percent mean absolute error (MAE) over a region of interest, defined as:

$$\text{bias} = \frac{\text{Mean}(\lambda_{E,v}) - \lambda_T}{\lambda_T} \times 100 \quad (14)$$

$$\text{MAE} = \text{Mean} \left(\frac{|\lambda_{E,v} - \lambda_T|}{\lambda_T} \right) \times 100 \quad (15)$$

where $\lambda_{E,v}$ is the value of the estimated parameter in voxel v, $\text{Mean}(\cdot)$ denotes the mean value over the voxels of the considered region, and λ_T is the corresponding true value of the parameter (uniform over the region). As for the Bayesian approaches, each $\lambda_{E,v}$ is taken as the expected value of the marginal posterior density in the voxel.

The noisiness of the map was evaluated considering the coefficient of variation (CV), calculated in each structure as the ratio between the standard deviation and the mean value of the parameters estimated in the considered region:

$$CV = \frac{\text{StD}(\lambda_{E,v})}{\text{Mean}(\lambda_{E,v})} \quad (16)$$

Being the true map uniform over the same structure, the ideal CV is 0; whilst high CV values indicate noisy maps.

An additional evaluation was performed on the simulated images at $\text{SNR} = 60$, considering a case with perfect knowledge to set the prior densities. Specifically, the Bayesian approaches were evaluated under a condition in which the mean values of the prior densities are equal to the true value of the parameters. Bias was thus calculated for this new condition, for each tissue and for each Bayesian method, together with the percentage variation (Var) between the true value, here adopted as mean value of the prior, and the mean value of the prior used in all other experiments.

2.3.2 | Real cases

The estimated parametric maps were qualitatively compared among the five methods, as a quantitative evaluation of the error cannot be performed in the absence of the true value of the IVIM parameters. For a quantitative evaluation, the measurements consistency across voxels was assessed in terms of the CV, calculated as in (16), and the goodness of fit was evaluated in each voxel (i, j) based on the Root Mean Square Error RMSE_{ij}:

$$\text{RMSE}_{ij} = \frac{\sqrt{\sum_{b \in B} (SI_{ijb}^{obs} - SI_{ijb}^{rec})^2}}{|B|} \quad (17)$$

where $|B|$ denotes the cardinality of set B and SI_{ijb}^{rec} the reconstructed value of $SI(i, j, b)$, computed with the IVIM model (1) and the estimated parameters. Then, the RMSE of a ROI was obtained by averaging the RMSE_{ij} values over the considered voxels.

3 | RESULTS

3.1 | Simulated images

The parametric maps in the HN region, estimated using the five methods, are presented in Figure 1, while the corresponding figure for the pelvis can be found in the Supporting Information Figure S3. The maps of fD^* (i.e., the product $f \times D^*$) are also represented in these figures, as such parameter shows a linear correlation with blood flow^{36,37}.

The estimated D maps were qualitatively acceptable for each method, except for the LSQ approaches at low SNR, which showed noisy images. The three Bayesian methods presented more homogeneous f maps with respect to the LSQ, even at low SNR. In the HN region, the map estimated by CAR at high SNR seemed to be the most similar to the true one, whereas, for the pelvis, the contrasts between tissues estimated by CAR, though similar to the real ones, were more blurred than with the other two Bayesian methods. The results of D* maps in HN highlighted the difficulty of the two GAUSS methods in correctly estimating muscle and parotid parameters, as can be observed by the inverted contrasts in these two layers. The two LSQ approaches presented a very high noise and, thus, the contrast between these two tissues was lost. On the contrary, the CAR method was able to both maintain the correct intensities and identify the two layers, though showing a blotchy appearance. Even in the pelvis, the CAR approach was the only one able of correctly recovering the contrast between tissues, as visible in the tumor, and at the same time estimating homogeneous maps.

Detailed results in terms of mean and standard deviation of each IVIM parameter calculated over the ROIs are reported in Table 1 for the HN region and in Supporting Information Table S3 for the pelvic region. Moreover, Figure 2 shows bias and CV in the HN region; the same Figure for the pelvic region, as well as results about MAE are extensively reported in Supporting Information Figures S4 and S5. LSQ-SEG achieved the best result for D in terms of bias ($\leq 1\%$, except in the prostate); on the contrary, CAR was the best in terms of MAE and CV (always less than 6% and 0.09, respectively), whilst LSQ-FULL resulted the worst estimator (bias up to -25% and CV up to 0.6 at low SNR). The other two Bayesian approaches reached acceptable errors, with bias $< 5\%$ for GAUSS-FULL and bias $< 2.5\%$ for GAUSS-SEG at high SNR. The worst estimation, for any method, was given in the prostate, where bias was higher (-25%, 4%, 9%, 4.5% and 3.5% for LSQ-FULL, LSQ-SEG, GAUSS-FULL, GAUSS-SEG and CAR, respectively) though the MAE values were in line with the other structures.

The estimation of f in the HN images highlighted the superiority of the Bayesian methods with respect to the LSQ at SNR = 20 and, more in general, the lower bias of the GAUSS-SEG and CAR. This behavior was less evident in the pelvis, where GAUSS-SEG presented higher errors at low SNR. CAR presented a bias $< 10\%$ and a MAE $< 12\%$ (excepted for the HN muscle and prostate at low SNR); at SNR > 60 also the other methods reached comparable bias, but the error and CV were always higher, or equal, than CAR, with very noisy maps for the LSQ approaches.

bias, MAE and CV in the estimation of D* in HN simulations were unacceptable for both LSQ methods, especially for muscle (bias $> 200\%$ for any SNR). CAR outperformed the other methods, showing the highest accuracy (maximum MAE and bias of 42% and -42% at SNR = 20 in muscle, otherwise they were always < 30 and 15%). GAUSS-SEG performed similar to or slightly better than GAUSS-FULL. CV values of the three Bayesian approaches were between 0.11 and 0.3, indicating less noisy maps, although the CAR, contrary to the others, showed some blotches instead of a high frequency noise. As for the pelvis, the general trend was confirmed in muscle and prostate; a specific comment should be dedicated to the tumor, which presented the worst bias for any method. Only the CAR was able to estimate the mean value with bias $< 26\%$ for SNR > 40 , whilst the others presented bias always greater than 80%, with the LSQ approaches that consistently overestimated the parameter and, on the contrary, the two GAUSS that underestimated it.

It is worth noting that the D and f values in HN muscle were always underestimated and overestimated, respectively, by each method, whilst D* was overestimated by LSQ approaches and underestimated by the Bayesian ones, independently from the SNR.

Var and bias in the two conditions (mean values of the priors set as described in Section 2.2 and as true tissue coefficients as described at the end of Section 2.3.1) are reported in Table 2. As expected, they showed lower bias values when the true coefficients were used, though they were still non-null. In particular, the two GAUSS methods seemed to be more influenced by the choice of the priors than the CAR approach, with a tendency of the GAUSS-SEG to reach lower differences between the errors computed in the two conditions and, in general, to be slightly less biased than the GAUSS-FULL. This rough evaluation highlighted that the CAR method is able to maintain low errors, similar to those obtained in the optimal condition, even with priors centered on values that are distant from the actual ones. In particular, large differences between the mean value of the prior densities and the actual tissue coefficients (difference between -33% and 40% for D, between -51% and 51% for f, and between -96% and 35% for D*) were experimented. In front of such large variations, the errors computed by the CAR were limited to a stricter range (between -1% and 4% for D, between -16% and 6% for f, and between -8% and 12% for D*).

3.2 | Real images

The parametric maps estimated from a real HN patient are shown in Figure 3 and in Supporting Information Figures S6-S8, while those from a real pelvic patient in Figure 4 and in Supporting Information Figures S9 and S10. In both regions, the three Bayesian methods provided the most smoothed and less noisy maps within the ROIs. A noisy and uncertain region outside the structures of interest can be observed for any fitting approach, although less evident for the two GAUSS methods. In fact, while the tissues within the ROIs were quite similar and homogeneous across the different methods, the outside regions were differently estimated. GAUSS methods generally estimated lower values for f and D* with respect to the LSQ and CAR approaches, while LSQ and CAR were qualitatively similar in terms of intensity levels, with a lower level of noise for CAR maps.

Looking at the estimated values of the three parameters (Table 3), D values were generally similar across the methods, while they were lower when estimated by LSQ-FULL. f presented a variation, on average, of 20% among LSQ-SEG, GAUSS-FULL, GAUSS-SEG and CAR, and it was always

at least 50% higher when estimated by LSQ-FULL. D^* was highly variable, with the highest mean values and standard deviations estimated by LSQ-FULL and LSQ-SEG. GAUSS-FULL and GAUSS-SEG always estimated the lowest D^* values, in agreement with the results found in the simulated images.

The CV values calculated in each structure are reported in Table 4; similar trends, with higher values, were in general found between the CV estimated in real images and those estimated from simulations. The CV for D was similar across the methods, except for LSQ-FULL which was always the highest. As for f and D^* , the LSQ-FULL and LSQ-SEG method always obtained the worst results, while GAUSS-FULL and GAUSS-SEG presented the lowest values. Contrary to the simulations, the CV values of f estimated by the CAR were higher than those by the two GAUSS approaches. These results were confirmed in both regions (HN and pelvis) for all the analyzed structures and in each subject.

RMSE in Table 4 and Figure 5 showed similar results across the methods, with a tendency of GAUSS approaches to reach the highest errors.

3.3 | Computational times

The average computational time was very different between LSQ and the Bayesian methods; with the actual programming languages used for the implementation it was 0.015 s/voxel for LSQ-FULL and 1.06 s/voxel for GAUSS-FULL. Moreover, segmentation increased the time of 13% (0.017 s/voxel) for LSQ-SEG and of 84% (1.96 s/voxel) for GAUSS-SEG with respect to the corresponding direct approach. Finally, the introduction of the CAR specification increased the time of about 8 times (9.86 s/voxel) with respect to the GAUSS-SEG. These times were obtained on a Unix machine equipped with CPU Intel Xeon Gold 5120 at 2.20GHz and 94 GB installed RAM.

4 | DISCUSSION

In this work a novel Bayesian approach was presented for the estimation of IVIM parametric maps, in two different versions: *i*) a segmented version of the classical Bayesian model with a Gaussian prior, and *ii*) an improvement of this one, where a spatial regularization term through a CAR specification was included in the prior density. These new approaches were compared with standard direct and segmented non-linear least-square methods and a classical direct Bayesian model with a Gaussian prior, considering both simulated and real images. To the best of our knowledge, a comparison between segmented and non-segmented Bayesian approaches is not available in the literature.

Looking at the simulated cases, it was found that, in general, the segmented approach in the Bayesian framework has brought some advantages with respect to the direct fitting, as the accuracy was slightly improved. The more significant improvement was given by the introduction of the CAR specification, which presented the lowest errors, in terms of both bias and MAE, and high homogeneity within the same tissue and that it was able to correctly recover the right contrasts between tissues in any condition. The performance of all approaches has proven to be dependent on SNR, though in some cases the bias was the same at any SNR, e.g., the estimation of D with each method or the estimation of f and D^* in parotid, pelvic muscle and prostate with the CAR method, for which the bias was very low for any SNR. In addition, a behavior opposite to what one should expect has been observed for the estimation of f in the prostate with the LSQ-SEG method, where the bias increased with SNR. It is worth noting that the maps estimated by CAR, although smooth and least biased, sometimes presented low-frequency noise, particularly in the D^* maps of HN simulations. These "blobs" are due to the smoothness of image noise, provided by the average on the neighbor pixels in the CAR specification, combined with the boundary-effect, where large difference in the exponential decay between different and neighbor structures may alter the estimate in voxels close to the edges. More details about this effect can be found in the Supporting Materials, where a comparison between the "step" simulations described in the previous sections and a "flat" simulation, without boundaries, is provided. The CAR method was also the only one able to estimate the D^* mean value in rectal tumor with small bias (bias lower than 10% for SNR60 and lower than then 40% for SNR40), whereas the two LSQ approaches consistently overestimated it and the two GAUSS underestimated it. This difficulty was probably due to the high difference between the mean value of the D^* prior density (0.01mm²/s) and its true value (0.257mm²/s). With such a large difference (−96% of variation with respect to the true value), only the CAR method seems robust enough to the choice of the prior hyper-parameters, as also highlighted in Table 2.

Regarding the real cases, the tissues within the regions of interest were quite similar and homogeneous across the different methods, whilst the outside regions were differently estimated. In fact, the estimation of diffusion parameters in certain tissues could be affected by the high level of noise, the very low signal or the presence of artifacts in these regions; moreover, D^* may be not properly defined where the perfusion compartment is vanishing, such as in teeth or fat³⁸. The D maps were consistent through the different methods within the ROIs, where LSQ-FULL was confirmed to estimate the noisiest maps, as shown in the simulations. Differences between LSQ-FULL and LSQ-SEG were more evident in pelvis than in HN, having the first higher CV that reflects noisy maps. Likewise, f maps within the three structures were similar, but the surrounding regions presented lower values when estimated by GAUSS-FULL and GAUSS-SEG, whilst CAR resulted less noisy than the two LSQ approaches. D^* maps were in line with the results on simulated images: LSQ-FULL, LSQ-SEG were the noisiest maps (in fact, they always presented the highest CV); again, the two GAUSS methods presented lower D^* values with respect to the other.

According to the results found in simulations, D^* estimated by CAR should be the least biased value. In fact, looking at the case of the HN muscle, the estimated D^* coefficients were in line with those reported in the simulations, considering similar SNR level. This is well visible also in Figure 3, where the muscle is hyper-intense in the CAR map and hypo-intense in the GAUSS maps. Since in the simulations the CAR was the most accurate, with a bias of -16% and a MAE of 27% at $\text{SNR} = 40$, which is close to the real SNR estimated in the muscle, it may be supposed that this accuracy was confirmed in the real images. In this sense, methods able to estimate more accurate maps can contribute to a better exploitation of the IVIM technique³⁹, as they may help in clarifying the biological interpretation of the IVIM coefficients. In fact, the potential clinical utility of the IVIM imaging in the tumor identification and characterization and in the prediction of treatment response has been already reported in several studies³⁸, and can be attributed to the added value provided from the IVIM parameters quantification. However, the biophysical interpretation of f and D^* is still not clear and thus the perfusion-related parameters are not considered by clinicians for tumor segmentation.

The two GAUSS methods seems to lose fine details within the considered ROIs, with respect to the LSQ approaches, as can be seen, for example, within the HN tumor in Figure 3. In fact, as reported by While¹⁹, Bayesian approaches can mask fine structures by generating smooth but erroneous portions of parametric maps. The same regions generally appear very noisy in LSQ maps, where a high level of uncertainty of the estimates is present. The lowest CV provided by the GAUSS methods may be interpreted in this sense: since lower CV in real images does not necessarily mean better maps, it could mask real heterogeneity present in the tissues. In addition, contrary to the results from simulated images, the CV values of f estimated by CAR were higher than those by the GAUSS approaches, thus highlighting that CAR might be able to preserve the real heterogeneity of tissues. However, looking at the results from the CAR method, the blotchy appearance of the maps, due to the smoothness of noise and to the boundary-effect between different and neighbor structures, may contribute to the disappearance of small subregions.

The RMSE analysis shows that CAR was not penalized by high errors, but it reached values similar to LSQ approaches, which presented the lowest RMSE, as expected¹⁹.

In all Bayesian approaches, prior densities were defined larger than in the literature. The rationale behind this choice was to define large prior distributions, in order not to force the posterior densities to be centered around predefined values. The Gaussian prior densities were centered on mean values with the same order of magnitude than the physiological values reported in the literature, as already performed in previous works²¹. This allows to define tissue-independent priors, which is particularly desirable when no other information about the true coefficients is available; in addition, to assume large densities, the standard deviations equal to the respective mean value have been taken. The results from the simulated images have highlighted that these large priors guarantee that the posterior densities are not very sensitive to the prior hyper-parameters. However, when the true value of the coefficients is far from the mean value of the initialization, the choice of the prior parameters may have a relevant impact, especially on GAUSS-FULL; in this case, it could be possible to easily change these hyper-parameters, either exploiting some a priori information, when available, or using a preliminary LSQ estimation on the signal averaged over the ROI.

Focusing on the benchmark models taken from the literature, the results of the LSQ methods are in line with the performance reported in the literature^{21,19,24,25}. In particular, in the simulated images, we have found that LSQ-FULL was generally less accurate in the parameters estimation than the LSQ-SEG approach, especially at low SNR. In the real cases, the CV of the LSQ-FULL approach was the worst for f and D^* estimation. From these results, and in agreement with a previous work⁴⁰, we may conclude that, if a least square approach is chosen, the segmented fitting should be preferred. Regarding the choice of constraints boundaries, here they were selected as adopted by While¹⁹, in order to have a more reliable comparison between the results presented here and those reported in the literature. Moreover, the choice of having large boundaries allows the methods to span across a large range of values, since four different structures were considered (parotid, tumor, prostate and muscle), and the tumors were very different between HN and rectal patients. An additional analysis (results not reported) on simulated HN images with tightened boundaries ($0 < f < 0.5$; $0 < D < 3 \times 10^{-3} \text{mm}^2/\text{s}$; $0 < D^* < 500 \times 10^{-3} \text{mm}^2/\text{s}$) has not shown any relevant improvement with respect to the larger constraints here adopted.

Looking at the errors reported by While¹⁹ for the Bayesian approach in liver (Error range: D 3-13%, f 3-10%, D^* 10-30%) and breast (Error range: D 3-13%, f 15-40%, D^* 25-50%), the results here reported were similar or even better. Even if a fair comparison between the two works was difficult, due to the different IVIM properties of the considered structures and the different acquisition protocols, we reported bias values lower than 10% in D and f maps (and often lower than 5% in D maps) for the most part of situations, for both GAUSS-SEG and CAR. Moreover, for CAR, a strong improvement in D^* was found in every structure and quite for every SNR if compared to the other three approaches (bias lower than 20% at high SNR, bias highly dependent on the considered structure at low SNR). The other two approaches already reported in literature, which considered a spatial homogeneity prior^{22,23}, presented some similarities to the CAR method, as they were all based on MRF with a neighborhood structure. However, the CAR approach here proposed was novel, as different from the previously cited methods for other aspects, especially in the implementation. The Bayesian approach here presented is not a pure CAR model (which can be traced to the MRF), but it is based on a mixture prior that includes both the CAR component and an independent truncated Gaussian prior in each voxel. The approach in^{22,23} includes the MRF together with a spatial homogeneity prior, which results in an energy minimization problem that is not treated with a Markov Chain Monte Carlo (MCMC) algorithm. To deal with the very high dimensionality of the parameters vector in their problem, the authors adopt a fusion bootstrap moves

algorithm, which is also the peculiarity and strength of their approach. On the contrary, the resulting model of our work can be treated with standard MCMC approaches (the Hamiltonian Monte Carlo in our case), with no need of ad hoc algorithms.

A direct comparison of the results here reported with those from similar approaches in the literature was difficult to perform, not only for the different implementation settings and the considered body districts, but also for the methods used to compute the errors. In fact, the median value over the ROI could be calculated instead of the mean value, as in¹⁹, in order to consider outliers or skewed distributions. bias and MAE of the LSQ approaches were particularly sensitive to the selected median or mean value metric, especially regarding the D^* maps, whereas the Bayesian approaches (and in particular the CAR) were less influenced, due to the Gaussian distribution of the IVIM coefficients over the ROI (results not shown in the manuscript). On the contrary, the distributions from the LSQ methods were not Gaussian at all, especially at low SNR values, with two high peaks both at very low and at very high (non-physiological) values, reflecting the noisy appearance of the maps with many spots. For such distributions, the median value over the ROI, though closer to the true value than the mean value, may mask this odd distribution. Thus, the computation of the mean value was preferred in this work, in combination with the CV, to give a synthetic description of accuracy and homogeneity in the estimated maps.

The adopted CAR is intrinsic (spatial association parameter ρ equal to 1 in the formulation of Leroux et al.³³). The use of the same prior knowledge of the GAUSS-FULL and GAUSS-SEG methods was preferred, in order to smooth the autoregressive component and to fix vague target values that the parameters have to follow. Alternatively, by simply reducing the correlation with $\rho < 1$, such target values would not appear in the model.

The CAR specification was preliminary tested in a non-segmented method, with different weights in the mixture prior: the 25 %, the 50 %, the 75% considered also in this paper and the 100% (i.e., a pure CAR method). Results (partly published in Lanzarone et al.⁴¹) showed saturation problems for the pure CAR alternative, especially for D^* , while acceptable results with the 75% weight, which were however worse than those obtained with segmentation in this paper. Moreover, those preliminary tests identified the adopted 75% weight as the best value, while the pure CAR method (with weight equal to 100%) did not work already at the first step.

The main limitation of the CAR method is in the choice of the neighbor voxels, which always considers all the eight surrounding voxels and gives the same weight to their contributions, without considering the continuity of the structure. For example, this affected the estimation of the coefficient close to the borders in the simulated images. In fact, different regions with different signal intensities at $b = 0$ could be characterized by similar decay dynamics, and vice versa. In the future, the CAR method will be coupled with a clusterization approach, to distinguish the different structures and give different weights to the contributions of the different neighbor voxels. Such a clustering will necessarily be based on distance functions that consider the differences between voxels over all b values, as single images cannot capture differences in the decay.

Another limitation is the long computational time of the Bayesian approaches, in particular the CAR. An optimization of these times, which would make the proposed methods more easily applicable to clinical protocols, could be achieved by decomposing the images in subparts or by implementing the methods with *ad hoc* codes rather than with package Rstan.

The focus of this work was on the comparison of the different approaches without considering the effects of the b values choice. In fact, the image acquisition protocols here adopted were already optimized for clinical purposes, especially for the HN acquisition. Since it was found that results were also dependent on the considered anatomical region, it is possible that the choice of b values plays a relevant role in the estimation performance of the five methods.

Another main limitation was the limited number of the analyzed clinical cases. However, this study was intended as a methodological proposal of the segmented Bayesian model combined with the CAR regularization; thus, a preliminary evaluation on simulated images was performed. We are confident that our findings, in terms of methods comparison, can be considered valid for the two analyzed regions. Obviously, an evaluation on an extended real dataset will be necessary for clinical purposes.

5 | CONCLUSIONS

It has been shown that the proposed segmented Bayesian approach was superior to the direct Bayesian method and to the standard least-square fitting, in terms of estimation accuracy and maps quality for f and D^* coefficients, in HN and pelvic regions. However, for D maps estimation only, LSQ-SEG may be preferred as the less biased method. Moreover, the use of large density prior did not affect the performance of the proposed segmented Bayesian approaches, allowing a sufficiently robust initialization. The CAR spatial regularization, in general, improves the estimation accuracy, especially for D^* , despite a slightly lower maps quality in the simulated images, due to the smoothing effect of noise and to the presence of functional gradients. However, future works will be directed to an optimized management of borders in the images, considering both anatomical and functional gradients, in order to face up this drawback and to recover high quality parametric maps.

ACKNOWLEDGEMENTS

Authors thank Dr. Simona Marzi of the Regina Elena National Cancer Institute, Rome, Italy, for her help in selecting the clinical cases.

SUPPORTING MATERIAL

Supporting Information Figures and Tables are provided in a separate document; the STAN implementation codes for the Bayesian approaches are provided in a .zip file.

References

1. Le Bihan Denis, Breton Eric, Lallemand Denis, Grenier Philippe, Cabanis Emmanuel, Laval-Jeantet Maurice. MR imaging of intravoxel incoherent motions: application to diffusion and perfusion in neurologic disorders.. *Radiology*. 1986;161(2):401–407.
2. Le Bihan Denis. Intravoxel incoherent motion imaging using steady-state free precession. *Magnetic resonance in medicine*. 1988;7(3):346–351.
3. Subhawong Ty K, Jacobs Michael A, Fayad Laura M. Insights into quantitative diffusion-weighted MRI for musculoskeletal tumor imaging. *American Journal of Roentgenology*. 2014;203(3):560–572.
4. Marzi Simona, Stefanetti Linda, Sperati Francesca, Anelli Vincenzo. Relationship between diffusion parameters derived from intravoxel incoherent motion MRI and perfusion measured by dynamic contrast-enhanced MRI of soft tissue tumors. *NMR in Biomedicine*. 2016;29(1):6–14.
5. Scalco Elisa, Marzi Simona, Sanguineti Giuseppe, Vidiri Antonello, Rizzo Giovanna. Characterization of cervical lymph-nodes using a multi-parametric and multi-modal approach for an early prediction of tumor response to chemo-radiotherapy. *Physica Medica*. 2016;32(12):1672–1680.
6. Nougaret Stephanie, Vargas Hebert Alberto, Lakhman Yulia, et al. Intravoxel incoherent motion-derived histogram metrics for assessment of response after combined chemotherapy and radiation therapy in rectal cancer: initial experience and comparison between single-section and volumetric analyses. *Radiology*. 2016;280(2):446–454.
7. Sakamoto Junichiro, Imaizumi Akiko, Sasaki Yoshinori, et al. Comparison of accuracy of intravoxel incoherent motion and apparent diffusion coefficient techniques for predicting malignancy of head and neck tumors using half-Fourier single-shot turbo spin-echo diffusion-weighted imaging. *Magnetic resonance imaging*. 2014;32(7):860–866.
8. Noij Daniel P, Martens Roland M, Marcus J Tim, et al. Intravoxel incoherent motion magnetic resonance imaging in head and neck cancer: A systematic review of the diagnostic and prognostic value. *Oral oncology*. 2017;68:81–91.
9. Marzi Simona, Forina Chiara, Marucci Laura, et al. Early radiation-induced changes evaluated by intravoxel incoherent motion in the major salivary glands. *Journal of Magnetic Resonance Imaging*. 2015;41(4):974–982.
10. Zhou Nan, Chu Chen, Dou Xin, et al. Early evaluation of irradiated parotid glands with intravoxel incoherent motion MR imaging: correlation with dynamic contrast-enhanced MR imaging. *BMC cancer*. 2016;16(1):865.
11. Marzi Simona, Farneti Alessia, Vidiri Antonello, et al. Radiation-induced parotid changes in oropharyngeal cancer patients: the role of early functional imaging and patient-/treatment-related factors. *Radiation Oncology*. 2018;13(1):189.
12. Levenberg Kenneth. A method for the solution of certain non-linear problems in least squares. *Quarterly of applied mathematics*. 1944;2(2):164–168.
13. Marquardt Donald W. An algorithm for least-squares estimation of nonlinear parameters. *Journal of the society for Industrial and Applied Mathematics*. 1963;11(2):431–441.
14. Byrd Richard H, Schnabel Robert B, Shultz Gerald A. Approximate solution of the trust region problem by minimization over two-dimensional subspaces. *Mathematical programming*. 1988;40(1-3):247–263.

15. Branch Mary Ann, Coleman Thomas F, Li Yuying. A subspace, interior, and conjugate gradient method for large-scale bound-constrained minimization problems. *SIAM Journal on Scientific Computing*. 1999;21(1):1–23.
16. Luciani Alain, Vignaud Alexandre, Cavet Madeleine, et al. Liver cirrhosis: intravoxel incoherent motion MR imaging—pilot study. *Radiology*. 2008;249(3):891–899.
17. Chandarana Hersh, Lee Vivian S, Hecht Elizabeth, Taouli Bachir, Sigmund Eric E. Comparison of biexponential and monoexponential model of diffusion weighted imaging in evaluation of renal lesions: preliminary experience. *Investigative radiology*. 2011;46(5):285–291.
18. Sigmund EE, Cho GY, Kim S, et al. Intravoxel incoherent motion imaging of tumor microenvironment in locally advanced breast cancer. *Magnetic resonance in medicine*. 2011;65(5):1437–1447.
19. While Peter T. A comparative simulation study of bayesian fitting approaches to intravoxel incoherent motion modeling in diffusion-weighted MRI. *Magnetic resonance in medicine*. 2017;78(6):2373–2387.
20. Neil Jeffrey J, Bretthorst G Larry. On the use of Bayesian probability theory for analysis of exponential decay date: an example taken from intravoxel incoherent motion experiments. *Magnetic resonance in medicine*. 1993;29(5):642–647.
21. Barbieri Sebastiano, Donati Olivio F, Froehlich Johannes M, Thoeny Harriet C. Impact of the calculation algorithm on biexponential fitting of diffusion-weighted MRI in upper abdominal organs. *Magnetic resonance in medicine*. 2016;75(5):2175–2184.
22. Freiman Moti, Perez-Rossello Jeannette M, Callahan Michael J, et al. Reliable estimation of incoherent motion parametric maps from diffusion-weighted MRI using fusion bootstrap moves. *Medical image analysis*. 2013;17(3):325–336.
23. Kurugol Sila, Freiman Moti, Afacan Onur, Perez-Rossello Jeannette M, Callahan Michael J, Warfield Simon K. Spatially-constrained probability distribution model of incoherent motion (SPIM) for abdominal diffusion-weighted MRI. *Medical image analysis*. 2016;32:173–183.
24. Gurney-Champion Oliver J, Klaassen Remy, Froeling Martijn, et al. Comparison of six fit algorithms for the intra-voxel incoherent motion model of diffusion-weighted magnetic resonance imaging data of pancreatic cancer patients. *PloS one*. 2018;13(4):e0194590.
25. Jalnefjord Oscar, Andersson Mats, Montelius Mikael, et al. Comparison of methods for estimation of the intravoxel incoherent motion (IVIM) diffusion coefficient (D) and perfusion fraction (f). *Magnetic Resonance Materials in Physics, Biology and Medicine*. 2018;;1–9.
26. Orton Matthew R, Collins David J, Koh Dow-Mu, Leach Martin O. Improved intravoxel incoherent motion analysis of diffusion weighted imaging by data driven Bayesian modeling. *Magnetic resonance in medicine*. 2014;71(1):411–420.
27. Suo Shiteng, Lin Naier, Wang He, et al. Intravoxel incoherent motion diffusion-weighted MR imaging of breast cancer at 3.0 tesla: comparison of different curve-fitting methods. *Journal of Magnetic Resonance Imaging*. 2015;42(2):362–370.
28. Sansone Mario, Fusco Roberta, Petrillo Antonella. D-optimal design of b-values for precise intra-voxel incoherent motion imaging. *Biomedical Physics & Engineering Express*. 2019;5(3):035025.
29. Duane Simon, Kennedy Anthony D, Pendleton Brian J, Roweth Duncan. Hybrid monte carlo. *Physics letters B*. 1987;195(2):216–222.
30. Team Stan Development, others . Stan modeling language users guide and reference manual. *Technical report*. 2016;.
31. Gudbjartsson Hákon, Patz Samuel. The Rician distribution of noisy MRI data. *Magnetic resonance in medicine*. 1995;34(6):910–914.
32. Gustafsson Oscar, Montelius Mikael, Starck Göran, Ljungberg Maria. Impact of prior distributions and central tendency measures on Bayesian intravoxel incoherent motion model fitting. *Magnetic resonance in medicine*. 2018;79(3):1674–1683.
33. Leroux Brian G, Lei Xingye, Breslow Norman. Estimation of disease rates in small areas: a new mixed model for spatial dependence. In: Springer 2000 (pp. 179–191).
34. Marzi Simona, Piludu Francesca, Vidiri Antonello. Assessment of diffusion parameters by intravoxel incoherent motion MRI in head and neck squamous cell carcinoma. *NMR in Biomedicine*. 2013;26(12):1806–1814.
35. Surov Alexey, Meyer Hans Jonas, Höhn Anne-Kathrin, et al. Correlations between intravoxel incoherent motion (IVIM) parameters and histological findings in rectal cancer: preliminary results. *Oncotarget*. 2017;8(13):21974.

36. Bihan Denis Le, Turner Robert. The capillary network: a link between IVIM and classical perfusion. *Magnetic resonance in medicine*. 1992;27(1):171–178.
37. Mastropietro Alfonso, Porcelli Simone, Cadioli Marcello, et al. Triggered intravoxel incoherent motion MRI for the assessment of calf muscle perfusion during isometric intermittent exercise. *NMR in Biomedicine*. 2018;31(6):e3922.
38. Federau Christian. Intravoxel incoherent motion MRI as a means to measure in vivo perfusion: A review of the evidence. *NMR in biomedicine*. 2017;30(11):e3780.
39. Vidić Igor, Jerome Neil P, Bathen Tone F, Goa Pål E, While Peter T. Accuracy of breast cancer lesion classification using intravoxel incoherent motion diffusion-weighted imaging is improved by the inclusion of global or local prior knowledge with bayesian methods. *Journal of Magnetic Resonance Imaging*. 2019;.
40. Park Hyo Jung, Sung Yu Sub, Lee Seung Soo, et al. Intravoxel incoherent motion diffusion-weighted MRI of the abdomen: The effect of fitting algorithms on the accuracy and reliability of the parameters. *Journal of Magnetic Resonance Imaging*. 2017;45(6):1637–1647.
41. Lanzarone Ettore, Scalco Elisa, Mastropietro Alfonso, Marzi Simona, Rizzo Giovanna. A conditional autoregressive model for estimating slow and fast diffusion from magnetic resonance images. In: Springer Proceedings in Mathematics & Statistics, vol. In press: Springer 2019 (pp. 1–10).

FIGURE LEGENDS

FIGURE 1. Parametric maps of D (top left), f (top right), D^* (bottom left) and product fD^* (bottom right) estimated from simulated images of the HN region using the five methods (rows) at different SNR (columns). The true maps are also reported besides.

FIGURE 2. Bias (a) and CV (b) in the maps of the simulated HN images for the D (first row), f (second row) and D^* (last row) in the three structures (muscle, first column; parotid, second column; tumor, last column).

FIGURE 3. Parametric maps of D (first row), f (second row), D^* (third row) and product fD^* (last row), estimated from the second selected slice of a real HN patient using the five methods (columns). The tumor, the parotid gland and the masticatory muscle were delineated in red, green and blue, respectively, also on the image at $b = 0$ reported on the left.

FIGURE 4. Parametric maps of D (first row), f (second row), D^* (third row) and product fD^* (last row), estimated from the first selected slice of a real pelvic patient using the five methods (columns). The tumor, the prostate and the internal obturator muscle were delineated in red, green and blue, respectively, also on the image at $b = 0$ reported on the left.

FIGURE 5. Maps of $RMSE_{ij}$ for the HN (first row) and the pelvic (second row) region for the patients in Figures 3 and 4, respectively, obtained by the five approaches; the three structures of interest are delineated in red.

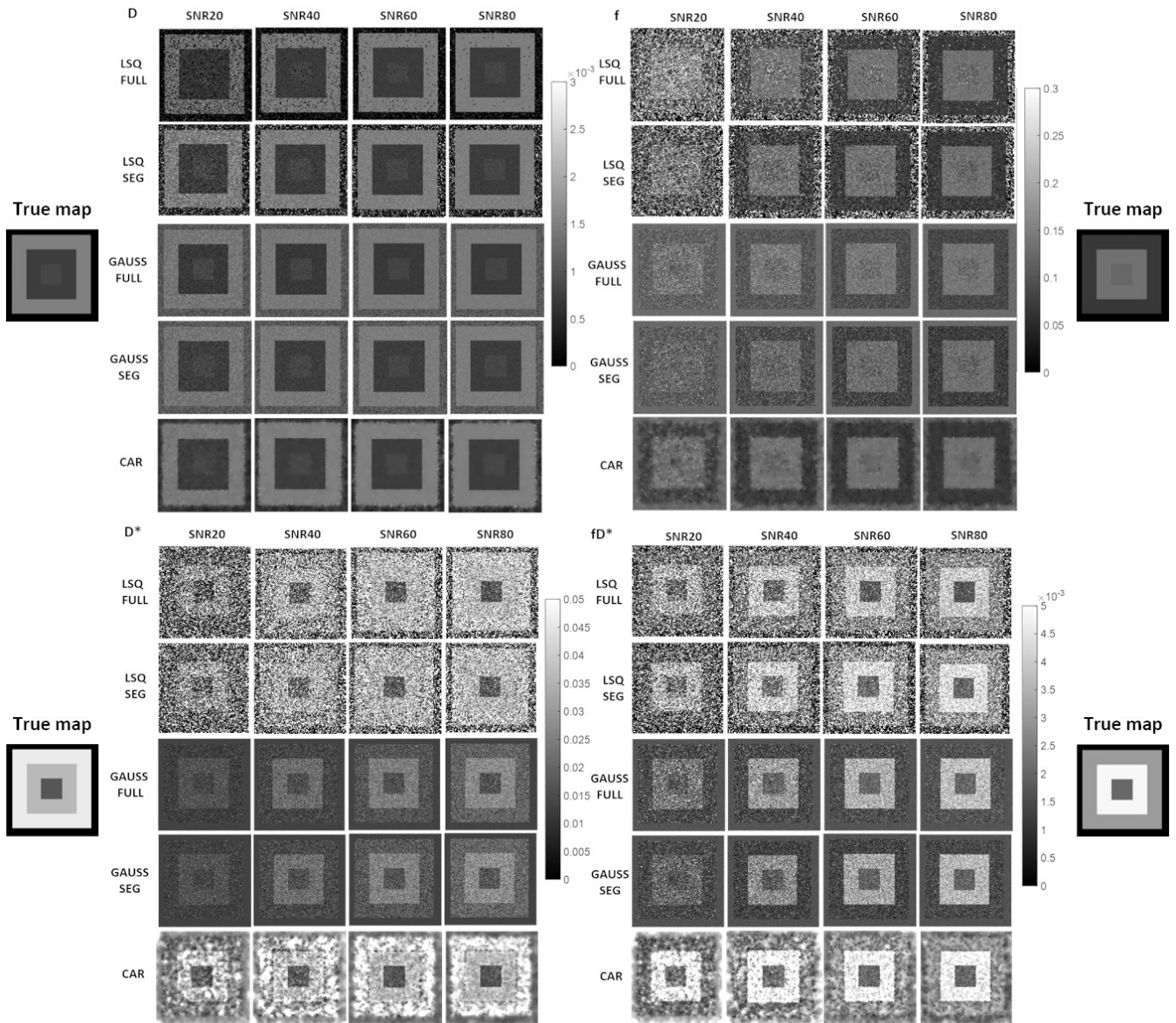


FIGURE 1 Parametric maps of D (top left), f (top right), D* (bottom left) and product fD* (bottom right) estimated from simulated images of the HN region using the five methods (rows) at different SNR (columns). The true maps are also reported besides.

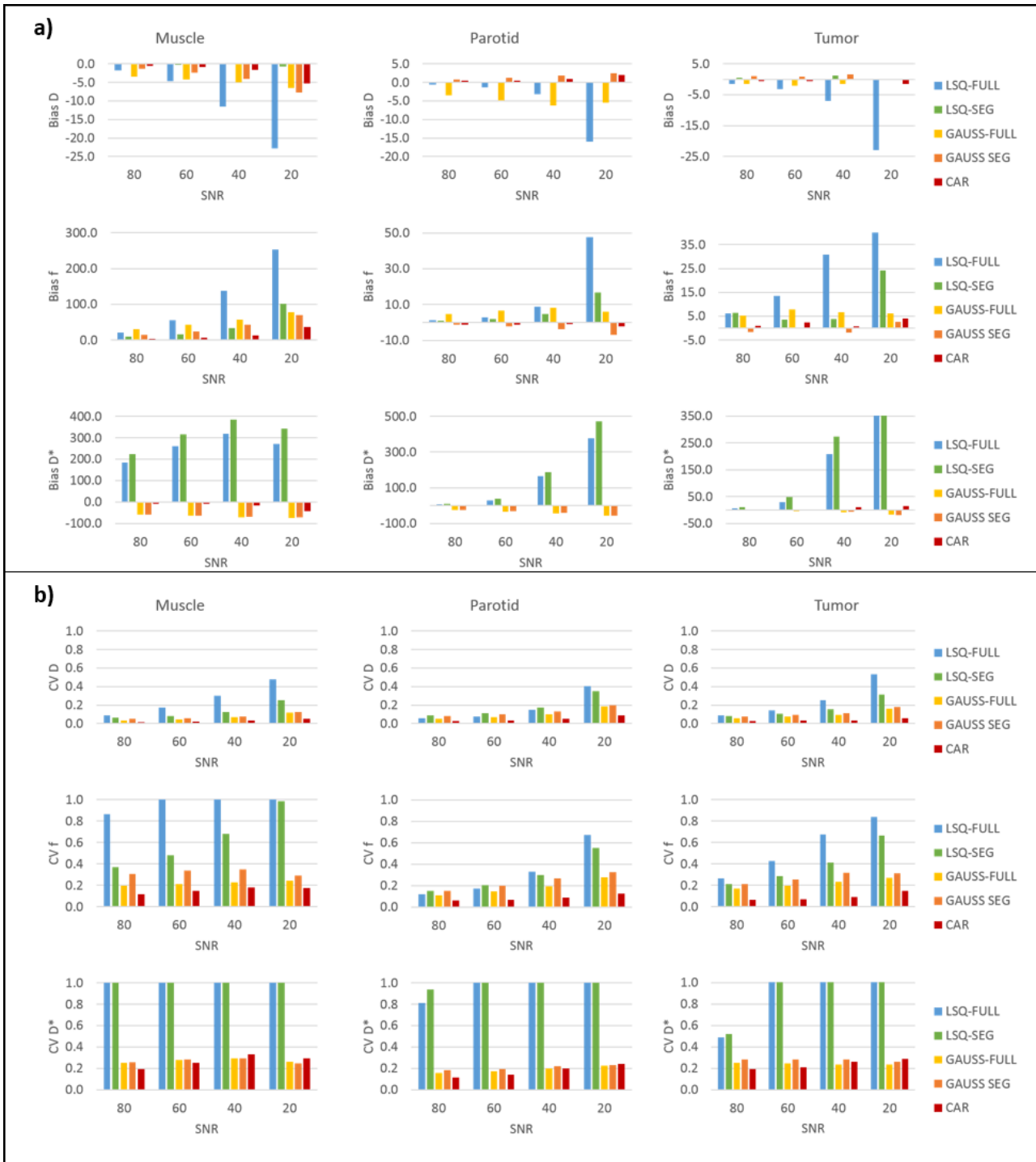


FIGURE 2 Bias (a) and CV (b) in the maps of the simulated HN images for the D (first row), f (second row) and D* (last row) in the three structures (muscle, first column; parotid, second column; tumor, last column).

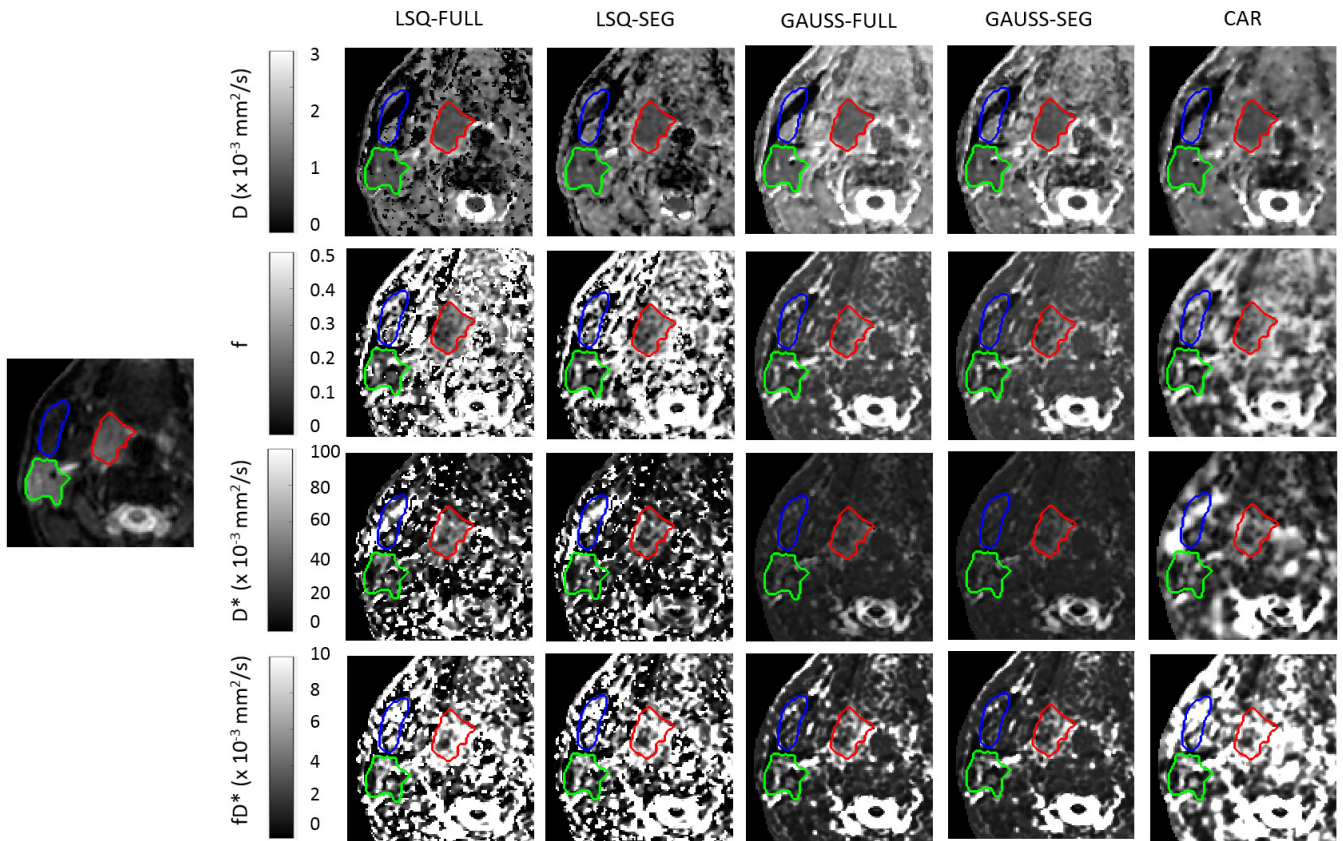


FIGURE 3 Parametric maps of D (first row), f (second row), D^* (third row) and product fD^* (last row), estimated from the second selected slice of a real HN patient using the five methods (columns). The tumor, the parotid gland and the masticatory muscle were delineated in red, green and blue, respectively, also on the image at $b = 0$ reported on the left.

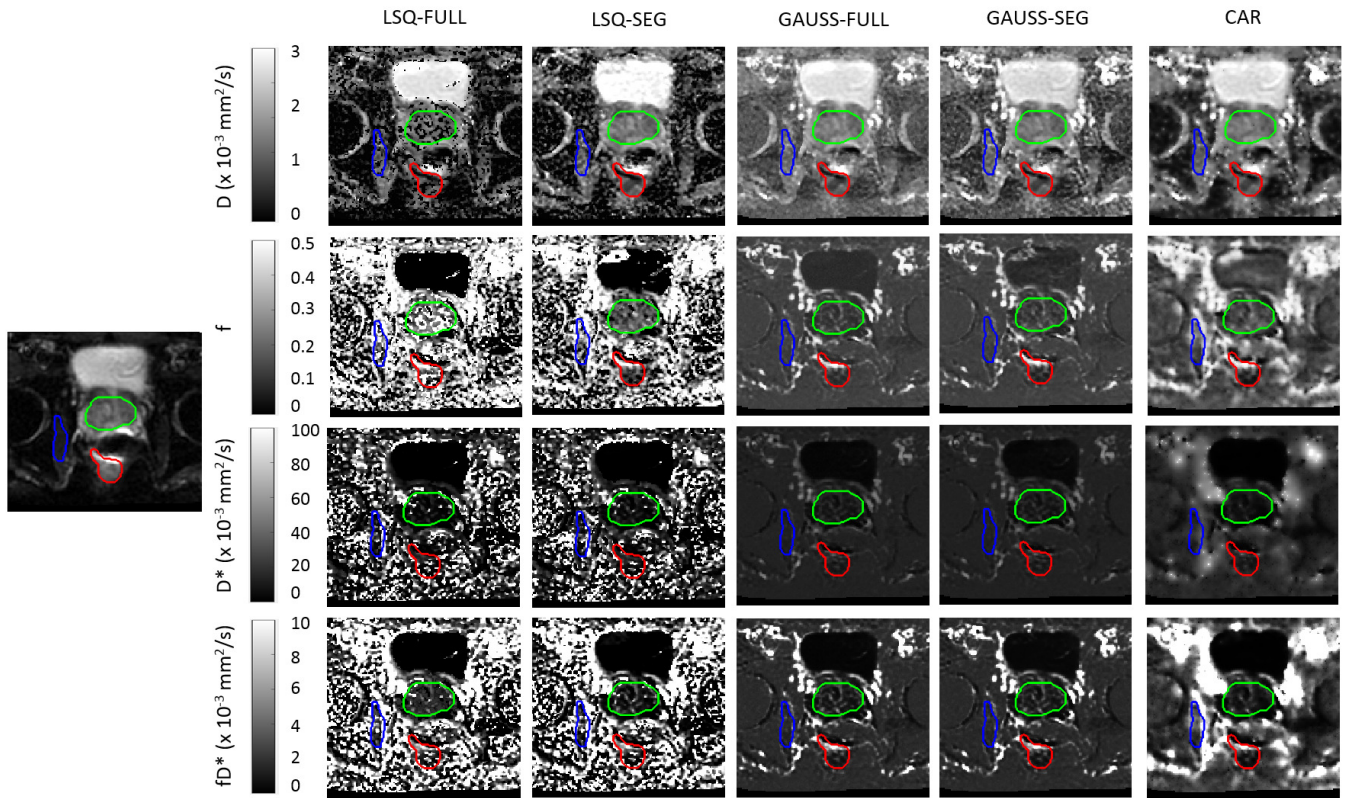


FIGURE 4 Parametric maps of D (first row), f (second row), D^* (third row) and product fd^* (last row), estimated from the first selected slice of a real pelvic patient using the five methods (columns). The tumor, the prostate and the internal obturator muscle were delineated in red, green and blue, respectively, also on the image at $b = 0$ reported on the left.

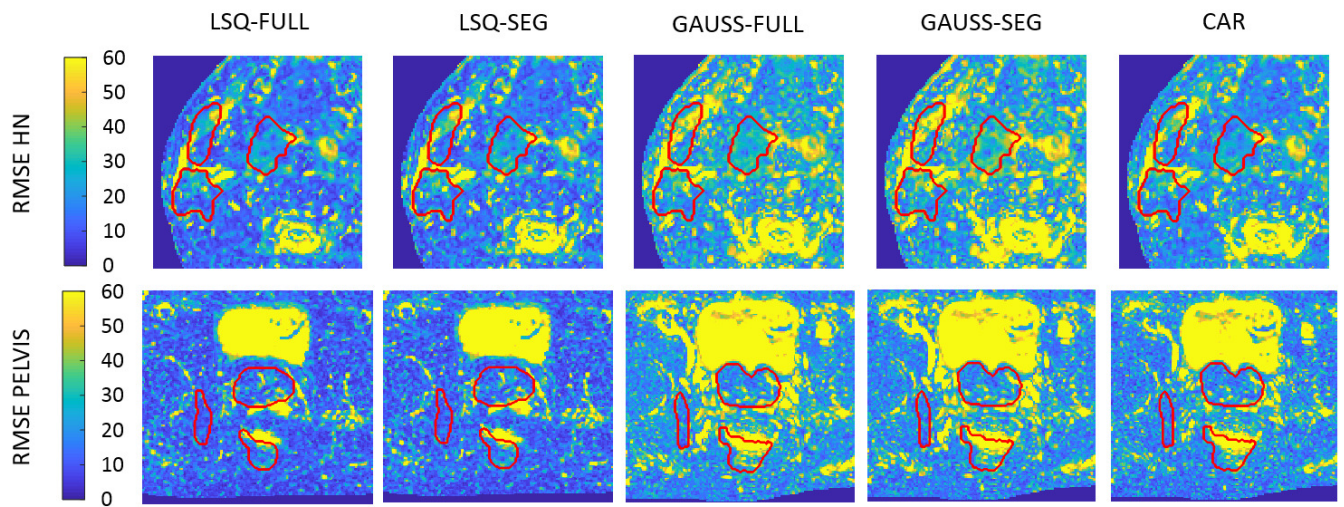


FIGURE 5 Maps of $RMSE_{ij}$ for the HN (first row) and the pelvic (second row) region for the patients in Figures 3 and 4, respectively, obtained by the five approaches; the three structures of interest are delineated in red.



		SNR = 80		SNR = 60		SNR = 40		SNR = 20		
		Mean	StD	Mean	StD	Mean	StD	Mean	StD	
HN muscle										
D	$1.5 \times 10^{-3} \text{mm}^2/\text{s}$	LSQ-FULL	1.49	0.13	1.48	0.24	1.45	0.40	1.36	0.55
		LSQ-SEG	1.50	0.09	1.49	0.12	1.49	0.19	1.48	0.38
		GAUSS-FULL	1.45	0.05	1.44	0.07	1.43	0.10	1.40	0.17
		GAUSS SEG	1.49	0.07	1.47	0.09	1.44	0.11	1.39	0.17
		CAR	1.50	0.03	1.49	0.03	1.48	0.05	1.43	0.08
f	0.066	LSQ-FULL	0.071	0.069	0.075	0.132	0.086	0.214	0.120	0.271
		LSQ-SEG	0.069	0.027	0.072	0.037	0.078	0.060	0.101	0.131
		GAUSS-FULL	0.085	0.017	0.092	0.020	0.100	0.024	0.111	0.029
		GAUSS SEG	0.072	0.023	0.078	0.028	0.089	0.033	0.107	0.032
		CAR	0.068	0.008	0.069	0.011	0.073	0.013	0.088	0.016
D*	$45.9 \times 10^{-3} \text{mm}^2/\text{s}$	LSQ-FULL	43.5	252.9	41.3	302.7	32.5	344.0	14.8	340.7
		LSQ-SEG	43.3	271.6	41.7	321.9	33.6	357.1	13.0	361.7
		GAUSS-FULL	19.4	4.9	16.4	4.6	13.7	4.1	12.1	3.3
		GAUSS SEG	20.4	5.2	17.4	4.9	14.5	4.3	12.6	3.2
		CAR	43.1	8.4	42.0	10.6	37.5	12.8	25.8	7.8
Parotid										
D	$0.72 \times 10^{-3} \text{mm}^2/\text{s}$	LSQ-FULL	0.72	0.04	0.71	0.06	0.71	0.10	0.66	0.25
		LSQ-SEG	0.72	0.06	0.72	0.08	0.72	0.12	0.72	0.25
		GAUSS-FULL	0.70	0.04	0.69	0.05	0.68	0.07	0.68	0.13
		GAUSS SEG	0.72	0.06	0.73	0.07	0.74	0.10	0.74	0.15
		CAR	0.72	0.02	0.72	0.02	0.72	0.04	0.73	0.07
f	0.133	LSQ-FULL	0.135	0.016	0.136	0.024	0.140	0.048	0.163	0.132
		LSQ-SEG	0.134	0.020	0.135	0.027	0.137	0.041	0.149	0.086
		GAUSS-FULL	0.140	0.015	0.142	0.020	0.144	0.028	0.136	0.039
		GAUSS SEG	0.132	0.020	0.130	0.026	0.127	0.034	0.120	0.040
		CAR	0.133	0.008	0.132	0.009	0.133	0.011	0.130	0.017
D*	$36.3 \times 10^{-3} \text{mm}^2/\text{s}$	LSQ-FULL	35.8	31.5	35.3	78.9	35.9	215.3	29.0	331.9
		LSQ-SEG	35.8	37.3	35.4	90.6	35.7	223.7	31.2	353.3
		GAUSS-FULL	27.2	4.3	24.6	4.3	21.2	4.3	16.2	3.7
		GAUSS SEG	28.1	5.1	25.8	4.9	22.1	4.8	16.3	3.8
		CAR	36.6	4.2	36.9	5.2	38.3	7.6	38.0	9.2
HN tumor										
D	$0.83 \times 10^{-3} \text{mm}^2/\text{s}$	LSQ-FULL	0.82	0.07	0.83	0.12	0.82	0.19	0.74	0.34
		LSQ-SEG	0.84	0.07	0.83	0.09	0.84	0.13	0.83	0.26
		GAUSS-FULL	0.82	0.05	0.82	0.06	0.82	0.07	0.83	0.13
		GAUSS SEG	0.84	0.06	0.84	0.08	0.85	0.10	0.83	0.15
		CAR	0.83	0.02	0.83	0.03	0.83	0.03	0.82	0.05
f	0.121	LSQ-FULL	0.123	0.034	0.128	0.059	0.131	0.107	0.167	0.200
		LSQ-SEG	0.120	0.027	0.124	0.036	0.121	0.052	0.137	0.100
		GAUSS-FULL	0.125	0.022	0.130	0.026	0.127	0.030	0.123	0.035
		GAUSS SEG	0.118	0.025	0.120	0.031	0.116	0.038	0.118	0.039
		CAR	0.122	0.008	0.123	0.009	0.122	0.011	0.126	0.019
D*	$16.9 \times 10^{-3} \text{mm}^2/\text{s}$	LSQ-FULL	16.1	8.7	16.3	49.3	16.3	160.2	11.9	236.0
		LSQ-SEG	16.3	9.7	16.0	69.9	17.5	182.1	13.7	282.6
		GAUSS-FULL	16.2	4.1	15.9	3.9	15.0	3.6	13.5	3.3
		GAUSS SEG	16.8	4.8	16.4	4.7	15.9	4.4	13.5	3.6
		CAR	16.8	3.2	17.1	3.6	18.6	4.9	19.2	5.6

TABLE 1 Values of D, f and D* estimated in each structure of interest by the five methods, for the simulated images in the HN region. Diffusion properties are reported as mean and standard deviation over the ROI. The true coefficients are also reported.

Tissue	D						f						D*					
	GAUSS-FULL		GAUSS-SEG		CAR		GAUSS-FULL		GAUSS-SEG		CAR		GAUSS-FULL		GAUSS-SEG		CAR	
	Var %	Bias %	Bias %	Bias %	Bias %	Bias %	Var %	Bias %	Bias %	Bias %	Bias %	Bias %	Var %	Bias %	Bias %	Bias %	Var %	Bias %
HN muscle	C1	-33.3	-4.3	-2.3	-0.9	-0.9	51.5	42.5	23.8	6.7	6.7	6.7	-78.2	-63.9	-62.4	-8.7		
	C2	0.0	-0.4	-1.0	-0.7	-0.7	0.0	5.3	8.3	4.5	4.5	4.5	0.0	27.5	21.2	2.2		
Parotid	C1	38.9	-4.9	1.2	0.5	0.5	-24.8	6.7	-2.1	-1.1	-1.1	-1.1	-72.5	-32.3	-30.1	1.0		
	C2	0.0	-0.6	0.1	0.3	0.3	0.0	0.9	0.2	-0.9	-0.9	-0.9	0.0	19.5	18.5	1.0		
HN tumor	C1	20.5	-2.1	0.8	-0.7	-0.7	-17.4	7.9	0.1	2.4	2.4	2.4	-40.8	-5.3	-2.1	1.1		
	C2	0.0	-1.1	0.2	-0.8	-0.8	0.0	6.2	1.7	1.6	1.6	1.6	0.0	16.9	16.3	-1.7		
Pelvic muscle	C1	-16.7	-1.7	1.8	0.0	0.0	-43.8	3.8	-2.3	0.0	0.0	0.0	-59.8	-15.2	-11.6	-6.2		
	C2	0.0	-0.1	0.4	-0.2	-0.2	0.0	0.9	0.0	0.1	0.1	0.1	0.0	12.0	10.3	-6.1		
Prostate	C1	-16.7	6.5	5.2	4.2	4.2	-40.1	-19.5	-21.0	-15.9	-15.9	-15.9	35.1	40.2	37.9	12.4		
	C2	0.0	2.5	4.4	3.9	3.9	0.0	6.2	-14.5	-14.5	-14.5	-14.5	0.0	4.3	15.9	4.3		
Rectal tumor	C1	-6.5	-5.6	2.7	1.7	1.7	-51.1	5.5	-1.7	-1.2	-1.2	-1.2	-96.1	-83.0	-83.1	0.5		
	C2	0.0	-0.3	0.7	1.4	1.4	0.0	0.1	-0.3	-1.2	-1.2	-1.2	0.0	39.7	37.7	10.7		

TABLE 2 Estimated bias for each tissue, using the three Bayesian approaches, in two conditions: C1 (mean values of the prior densities D, f, D^* and D_{sum} equal to $0.001\text{mm}^2/\text{s}, 0.1, 0.01\text{mm}^2/\text{s}$ and $0.011\text{mm}^2/\text{s}$, respectively) and C2 (mean values of the prior densities equal to the true coefficient of each tissue). Results refer to the simulated images with $\text{SNR} = 60$.

		D [mm ² /s]		f		D* [mm ² /s]	
		Mean	StD	Mean	StD	Mean	StD
HN region							
Muscle	LSQ-FULL	0.0013	0.0004	0.2336	0.0682	0.1066	0.0204
	LSQ-SEG	0.0016	0.0005	0.1814	0.0684	0.1240	0.0083
	GAUSS-FULL	0.0015	0.0004	0.1586	0.0276	0.0151	0.0024
	GAUSS-SEG	0.0015	0.0004	0.1458	0.0229	0.0151	0.0020
	CAR	0.0015	0.0005	0.1691	0.0621	0.0341	0.0069
Parotid	LSQ-FULL	0.0009	0.0001	0.2727	0.0425	0.1378	0.0405
	LSQ-SEG	0.0010	0.0001	0.2140	0.0421	0.1320	0.0363
	GAUSS-FULL	0.0011	0.0001	0.1835	0.0277	0.0189	0.0035
	GAUSS-SEG	0.0011	0.0001	0.1782	0.0275	0.0184	0.0035
	CAR	0.0011	0.0001	0.1994	0.0354	0.0378	0.0084
Tumor	LSQ-FULL	0.0008	0.0002	0.2564	0.0867	0.1250	0.0569
	LSQ-SEG	0.0009	0.0001	0.1728	0.0849	0.1332	0.0681
	GAUSS-FULL	0.0010	0.0002	0.1556	0.0558	0.0163	0.0035
	GAUSS-SEG	0.0010	0.0001	0.1505	0.0639	0.0162	0.0034
	CAR	0.0009	0.0001	0.1631	0.0777	0.0421	0.0235
Pelvic region							
Muscle	LSQ-FULL	0.0009	0.0006	0.3956	0.3776	0.0677	0.2315
	LSQ-SEG	0.0014	0.0003	0.1692	0.1523	0.0685	0.2285
	GAUSS-FULL	0.0014	0.0001	0.1288	0.0049	0.0125	0.0005
	GAUSS-SEG	0.0013	0.0002	0.1268	0.0049	0.0128	0.0005
	CAR	0.0013	0.0001	0.1331	0.0238	0.0131	0.0012
Prostate	LSQ-FULL	0.0009	0.0005	0.3334	0.3088	0.0710	0.2201
	LSQ-SEG	0.0012	0.0002	0.1455	0.1137	0.0781	0.2257
	GAUSS-FULL	0.0013	0.0002	0.1279	0.0120	0.0127	0.0010
	GAUSS-SEG	0.0012	0.0003	0.1262	0.0105	0.0129	0.0009
	CAR	0.0012	0.0003	0.1500	0.0551	0.0148	0.0073
Tumor	LSQ-FULL	0.0007	0.0004	0.2211	0.2628	0.0930	0.2500
	LSQ-SEG	0.0009	0.0003	0.1036	0.0688	0.0584	0.1913
	GAUSS-FULL	0.0009	0.0003	0.1194	0.0399	0.0128	0.0058
	GAUSS-SEG	0.0009	0.0003	0.1154	0.0464	0.0129	0.0057
	CAR	0.0009	0.0003	0.1137	0.0533	0.0167	0.0132

TABLE 3 Values of D, f and D* estimated in each structure of interest by the five methods, for the real images. Diffusion properties are reported as mean and standard deviation across subjects.

		CV of D		CV of f		CV of D*		RMSE	
		Mean	StD	Mean	StD	Mean	StD	Mean	StD
HN region									
Muscle	LSQ-FULL	0.46	0.27	1.04	0.37	2.48	0.27	23.6	8.8
	LSQ-SEG	0.32	0.23	0.95	0.31	2.28	0.10	26.8	10.4
	GAUSS-FULL	0.28	0.21	0.47	0.04	0.36	0.05	31.9	9.2
	GAUSS-SEG	0.31	0.18	0.43	0.03	0.32	0.05	33.5	8.7
	CAR	0.29	0.20	0.59	0.14	0.62	0.12	28.5	9.2
Parotid	LSQ-FULL	0.53	0.10	0.86	0.06	2.22	0.39	25.8	6.1
	LSQ-SEG	0.32	0.08	0.77	0.04	2.24	0.31	28.9	7.2
	GAUSS-FULL	0.44	0.15	0.54	0.03	0.53	0.07	35.8	9.8
	GAUSS-SEG	0.42	0.08	0.55	0.06	0.52	0.08	39.1	9.3
	CAR	0.40	0.11	0.58	0.06	0.91	0.24	31.3	8.1
Tumor	LSQ-FULL	0.57	0.22	0.97	0.37	2.38	0.41	30.8	15.1
	LSQ-SEG	0.34	0.17	0.81	0.31	2.28	0.43	33.0	14.5
	GAUSS-FULL	0.30	0.10	0.50	0.14	0.51	0.21	36.7	13.4
	GAUSS-SEG	0.29	0.09	0.54	0.15	0.48	0.21	37.7	12.8
	CAR	0.29	0.10	0.63	0.20	0.92	0.29	32.7	14.8
Pelvic region									
Muscle	LSQ-FULL	0.65	0.07	0.95	0.07	2.85	0.60	13.3	1.6
	LSQ-SEG	0.30	0.09	0.84	0.06	2.72	0.62	14.4	1.6
	GAUSS-FULL	0.12	0.04	0.12	0.05	0.11	0.05	20.3	3.1
	GAUSS-SEG	0.18	0.04	0.10	0.04	0.10	0.04	19.1	2.5
	CAR	0.14	0.04	0.29	0.09	0.30	0.15	18.8	2.9
Prostate	LSQ-FULL	0.63	0.06	0.86	0.09	3.92	1.16	17.8	1.7
	LSQ-SEG	0.19	0.02	0.63	0.21	3.72	1.18	18.6	1.4
	GAUSS-FULL	0.15	0.01	0.16	0.09	0.16	0.12	28.1	3.2
	GAUSS-SEG	0.21	0.08	0.15	0.10	0.16	0.12	25.7	1.5
	CAR	0.21	0.08	0.32	0.06	0.47	0.03	25.2	1.7
Tumor	LSQ-FULL	0.62	0.12	1.01	0.18	2.83	0.56	39.0	10.4
	LSQ-SEG	0.40	0.12	0.85	0.18	2.83	0.68	40.5	10.6
	GAUSS-FULL	0.43	0.09	0.53	0.14	0.51	0.13	45.0	10.5
	GAUSS-SEG	0.40	0.10	0.58	0.14	0.51	0.15	44.7	11.2
	CAR	0.40	0.10	0.59	0.11	0.80	0.21	42.6	10.7

TABLE 4 CV and RMSE values obtained in each structure of interest by the five methods, for the real images. Values are reported as mean and standard deviation across subjects.